Title
CO2 injection-induced fracturing in naturally fractured shale rocks

Authors
Wang, Lei
Yao, Bowen
Xie, Haojun
et al.

Publication Date
2017-11-01

DOI
10.1016/j.energy.2017.08.031

Peer reviewed

CO_2 injection-induced fracturing in naturally fractured shale rocks

Lei Wang[a], Bowen Yao[a], Haojun Xie[a,b], Philip H. Winterfeld[a], Timothy J. Kneafsey[c], Xiaolong Yin[a], Yu-Shu Wu[a]

[a]Petroleum Engineering Department, Colorado School of Mines; [b]College of Petroleum Engineering, China University of Petroleum (East China); [c]Earth Science Division, Lawrence Berkeley National Laboratory.

The first two authors contributed equally to this study.

Abstract

Niobrara shale cubes of 20 cm from Colorado were employed to investigate gas and supercritical CO_2 injection-induced fracturing in naturally fractured caprocks of deep aquifers/depleted reservoirs and fractured shale reservoirs. Under tri-axial stresses, gas or supercritical CO_2 was injected into the center of the cubes to induce fracturing. Real-time pressure and temperature, acoustic wave, pressure decay, fracture coloring, and gas fracturing were used to characterize the fracturing process and fracture morphology. Without pore pressure, CO_2 injection-induced fracturing occurred and completed instantly, accompanied by an evident temperature drop. Strongly bonded fractures barely affected transverse fracture propagation, whereas weakly bonded or open fractures arrested the injected fluid first and then allowed it to generate new fractures perpendicular to the minimum horizontal stress. Breakdown pressures for cubes with preexisting fractures using gas and supercritical CO_2 are much lower than both poroelastic predictions and slick-water fracturing pressure, and some are even lower than the minimum horizontal stress. This is attributed to unconformable preexisting fractures and the low viscosity of CO_2. Moreover, decreasing tri-axial stress levels and increasing stress differences tend to lower the breakdown pressure. This study is instructive for understanding and tackling geomechanical issues related to CO_2 geological storage and fracturing of shale reservoirs.

Keywords: supercritical CO_2, injection-induced fracturing, shale, natural fracture, true tri-axial stress, breakdown pressure

Introduction

In reducing anthropologic CO_2 emission from power plants and other industrial applications, a series of technologies for carbon capture, utilization, and storage (CCUS) have been developed and implemented during the past half century (GCI 2016). CO_2 capture can be carried out during different stages of the fuel combustion as pre-combustion, oxy-fuel combustion, and post-combustion processes (Mondal et al. 2012). And several capture techniques have been successfully applied in coal-fired power plants, such as the solvent adsorption process for capturing CO_2 from flue gas using amine compounds (Hirata et al. 2014).

Lately, more high-efficiency CO_2 capture sorbents have been found and systematically investigated, for example, the K_2CO_3/Al_2O_3 sorbent possessing fast reaction and high carbonation conversion rate with respect to CO_2 in flue gas (Zhao et al. 2012a, 2012b). After capture, CO_2 is generally separated and sorbents are regenerated. Then, utilization and storage are two different destinations for the captured CO_2, the former treats CO_2 as a feed stock for synthesizing new chemicals and producing fuels, or an environmentally friendly vehicle for enhanced oil/gas recovery (Iribarren et al. 2013), while the latter compresses, transports, and injects CO_2 into a proper geological site for long-term sequestration (Cuéllar-Franca and Azapagic 2015). It is obvious that utilization provides beneficial options of turning CO_2 into high-demand products or entering life cycles of different industrial applications, whereas storage is only an unprofitable fate for captured CO_2 requiring additional pipeline construction, well drilling, and energy consumption (Esposito et al. 2013, Koperna, Jr. 2013). Nonetheless, most utilization options do not have sufficient capacity to mitigate CO_2 emission and are temporary regarding the life cycles of the products. Geological sequestration and storage in deep saline aquifers and oil and gas reservoirs, on the other hand, is a permanent solution with enormous capacity and worldwide availability, though accompanied by leakage risk (Buttinelli et al. 2011, Vulin et al. 2012, Pham et al. 2013). On sites overlapping with oil and gas fields, abundant surface / subsurface facilities and geological features can be exploited, and the whole process could even be more practical and economical provided the CO_2 enhanced oil recovery benefit. For safe and permanent CO_2 geological storage, the caprock overlying the storage formation should be intact and integrated so that CO_2 can be effectively trapped without escape. In addition, the subsurface plumes of sequestrated CO_2 should be continuously monitored to ensure that containment is provided. These are not only technological prerequisites but also required by federal laws and regulations, e.g. in the United States.

Exemplary CO_2 geological storage projects

In recent years, several field-scale CO_2 storage projects have been implemented around the world, for example, the injection in the Sleipner offshore field in the North Sea of Norway (Zweigel et al. 2004) and the injection in In Salah field in Algeria (Iding and Ringrose 2010, Rutqvist et al. 2010). Both of these projects inject CO_2 separated from the produced natural gas stream; the difference is that the Sleipner project injects CO_2 into a ~250 m thick sandstone aquifer (Utsira formation) above the gas reservoir (Zweigel et al. 2004), while the In Salah project injects CO_2 into the ~20 m thick brine-saturated flank of the gas reservoir (White et al. 2014). The Sleipner project started in September 1996 and until June 2016, about 16.2 million tons of CO_2 had been sequestered. The caprock of the Utsira formation is considered effective in sealing so that the injection is still ongoing (GCI, 2017). The In Salah project started in 2004, in total, over 3.8 million tons of CO_2 had been sequestered until its suspension in June 2011, out of concern over the integrity of the ~150 m sublayer right above the storage formation. But the

sealing integrity of the other ~800 m caprock above this sublayer is not thought to be impaired (Ringrose 2013). The permeability ranges of Sleipner and In Salah injection zones are 1-3 Darcy (Chadwick et al. 2004) and 1-100 milli-Darcy (Iding and Ringrose 2010), respectively. Together with the big difference in thickness, the In Salah storage formation is more geomechanically susceptible given the reported amount of injected CO_2, which has been verified by rate- and pressure-correlated microseismic events (Oye et al. 2013), surface lifts from satellite-based geodetic measurements (Vasco et al. 2010), coupled geomechanics and fluid flow simulation (Rutqvist et al. 2010), etc. Note that the injection pressure in In Salah storage formation is around 300 bar and the bottom hole temperature is about 40 °C lower than the formation temperature of 93 °C (Bissell et al. 2011), both above the supercritical point (1070.4 psi and 31.0 ºC) of CO_2 (Suehiro et al. 1996). Though lacking field data with high confidence renders the interpretations difficult, it is generally believed that fracturing was induced in the ~150 m caprock sublayer containing preexisting fractures by high-pressure CO_2 injection (Iding and Ringrose 2010, White et al. 2014).

By means of numerical simulation, several studies tried to evaluate the fracturing processes induced during CO_2 injection into storage formations (e.g. Pan et al. 2013, Rinaldi et al. 2014, Zhang et al. 2016). Huang et al. (2015) set preexisting fractures in storage reservoirs to simulate supercritical (sc) CO_2 injection pressure responses for monitoring purposes by coupling thermal, hydraulic, and mechanical processes. They suggested that installing downhole pressure gauges should be useful to quantify $scCO_2$ leakage pathways and rates, and that increasing the injection rate slowly would reduce the caprock rock failure risks. In laboratory, studies on $scCO_2$ induced fracturing processes are limited. Ishida et al. (2012, 2016) and Chen et al. (2015) injected $scCO_2$ into 17 cm granite cubes under tri-axial stresses and observed that $scCO_2$ created more tortuous and branched fractures with lower breakdown pressures than oil and water of higher viscosity. Under simple tri-axial stress conditions, Li et al. (2016) fractured cylindrical Green River shale samples and obtained marginally more complex fracture patterns with CO_2 than water. Zhang et al. (2017) recently conducted water, liquid CO_2, and $scCO_2$ fracturing on 20 cm shale cubes obtained from the outcrop of the Lower Silurian Longmaxi Formation in Sichuan Basin, China. Their experiments demonstrated that the breakdown pressure of the shale samples decreased significantly with the decreasing fluid viscosity, and specifically that of $scCO_2$ fracturing was about half of that of water fracturing. In addition, the $scCO_2$ induced fractures are more irregular and have more small cracks than hydraulic fractures. In consideration of shale or mudstone caprocks with preexisting faults and fractures, there are quite a few discussions regarding fault reactivation and seismicity triggering (Zoback and Gorelick 2012, Vilarrasa and Carrera 2015). However, $scCO_2$ injection-induced fracturing processes and mechanisms are still not very clear, particularly direct experimental observations on real caprocks are very rare.

Hydraulic fracture initiation

Hydraulic fracturing processes have been widely investigated with conventional reservoir rocks or analogs. In general, the factors that affect fracture initiation in homogeneous reservoir rocks mainly include *in-situ* (confining) stress, fracturing fluid pressure (Hubbert and Willis 1957), fluid leak off, tensile strength, and other rock properties (Haimson and Fairhurst 1967), which can be correlated to the fracture initiation pressure by the following equations at different conditions.

When no fluid leak off is assumed, the fracture initiation or breakdown pressure can be calculated by (Hubbert and Willis 1957)

$$P_b = 3\sigma_h - \sigma_H + \sigma_t - P_p \tag{1}$$

where σ_h and σ_H are the minimum and maximum horizontal stresses, respectively; σ_t is the tensile strength of the reservoir rock, and P_p is the pore pressure.

If the reservoir rock is permeable, then the fracture initiation pressure can be obtained from (Haimson and Fairhurst 1967, Detournay and Cheng 1992)

$$P_b = \frac{3\sigma_h - \sigma_H + \sigma_t - \alpha(1-2\upsilon)/(1-\upsilon)\times P_p}{2-\alpha(1-2\upsilon)/(1-\upsilon)} \tag{2}$$

where α is Biot's constant and υ is Poisson's ratio.

Ideally within homogeneous reservoirs, hydraulic fracturing is dominated by *in-situ* stress and fractures typically initiate perpendicular to the minimum horizontal stress direction. Nonetheless, actual reservoir heterogeneity, wellbore perforations, well orientation relative to principal stresses, and so on can all alter the local stress distribution, and the direction of fracture initiation.

Hydraulic fracture propagation

Compared to fracture initiation, propagation is less susceptible to the restrained local stress alternation. During fracture propagation, the fracture planes should be perpendicular to the minimum horizontal stress, as has been verified by many theoretical and experimental investigations (Hubbert and Willis 1957, Hanson et al. 1980). Given a sensible difference

between the maximum and minimum horizontal stresses, the fracture plane always turns to be perpendicular to the minimum horizontal stress as it propagates into the reservoir, even though the initiation direction might be different (Tyler and Vollendorf 1975).

Hydraulic fracture propagation pressure is generally lower than the initiation pressure, depending on the stress states near the fracture tip and the fluid pressure inside it. Linear elasticity shows that there exists a critical stress intensity factor K_{Ic} for Mode I fracturing of a material (Irwin 1957)

$$K_{Ic}=\sqrt{\frac{2E\gamma}{1-\upsilon^2}} \tag{3}$$

where *E* is Young's modulus and γ is the specific surface energy.

K_{Ic}, as a material constant, can either be measured experimentally or calculated theoretically (Sneddon 1946). When the actual stress intensity factor exceeds K_{Ic}, fracture is expected to propagate. For a fracture in 2D geometries, the intensity factor is

$$K_I=\left(P_f-\sigma_h\right)\sqrt{\pi L_f} \tag{4}$$

where P_f is the fluid pressure in the fracture tip and L_f is the fracture half length.

And for a circular fracture in 3D geometries, the intensity factor is

$$K_I=\frac{2}{\pi}\left(P_f-\sigma_h\right)\sqrt{\pi R_f} \tag{5}$$

where R_f is the fracture radius (Liu 2016).

Combining equations (3) and (5), one can easily obtain the fracturing fluid pressure needed for propagating a fracture in homogeneous reservoir rocks. Obviously, the required

pressure is a function of σ_h, fracture mode and size, and rock properties. Specifically, it increases with increasing σ_h and decreasing fracture size. Note that fluid leak off that reduces the intensity factor is not considered in equations (4) and (5). Equations (3) to (5) are only applicable for intact and homogeneous reservoir rocks, but as a matter of fact, reservoir rocks are mostly heterogeneous and contain numerous fractures.

Effect of preexisting fractures on hydraulic fracturing

Naturally, most geological formations experienced complex sedimentary processes, tectonic activities, diagenetic evolution, reservoir pressure changes, and so on. Thus, rock properties of sublayers are generally different from each other, and faults and fractures are ubiquitous in geological formations at different scales (Sonnenberg 2012, Gale et al. 2014). In addition, considering CO_2 storage in oil and gas reservoirs, pressure depletion due to production generally results in subsidence of the overburden formations, which could result in disintegration or fracturing of the caprocks over conventional reservoirs. In unconventional reservoirs, besides the natural fractures, hydraulic fractures are often created for improving hydrocarbon recovery by injecting fracturing fluids.

The preexisting faults, fractures, and weak layer interfaces could have a strong influence on the hydraulic fracture propagation in real situations such that the propagating fractures could either be inhibited, promoted, arrested, or reoriented in terms of the bonding strength and orientation of the fractures or interfaces. Strong bonding interfaces not parallel to the fracture propagation will increase the fracturing pressure, and eventually allow the fractures to propagate through them (Daneshy 1978). Weakly bonded fractures, if in coincidence with the orientation of fracture extension, will facilitate the hydraulic fracture propagation. Weakly bonded fractures not parallel to the fracture extension will probably arrest the fracture propagation (Daneshy 1974). Nonetheless, given increasing hydraulic pressure, fractures reoriented along the weakly bonded interface could again return to the original orientation dominated by the *in-situ* stresses.

Therefore, to optimize the practical operations in the field, discussing the presence of preexisting fractures during $scCO_2$ injection is inevitable and meaningful. At present, there are very few investigations that target the effect of preexisting fractures on $scCO_2$ injection-induced fracturing of caprocks, i.e. shale or mudstone.

In this study, we acquired shale rock chunks from the CEMEX Lyons cement plant, where the Niobrara shale outcrop is excavated as a raw material to manufacture Portland cement. From the sub-meter scale chunks, we have cut five 20 cm shale cubes, within which natural or

preexisting fractures were observed. For some of the shale cubes, visible natural fractures or interfaces were bonded with epoxy. In total, three types of shale cubes with preexisting fractures of different bonding strength were prepared: a) Natural calcite-filled or strongly bonded fractures, b) Preexisting open / unbonded fractures, c) Weakly epoxy bonded fractures. By varying the tri-axial stresses, we injected CO_2 into four shale samples and slick-water into one sample to investigate the initiation, propagation, patterns, and morphology of injection-induced fractures.

Shale sample preparation

All shale samples were cut nearly perpendicular to the bedding planes, and boreholes were drilled 11.43 cm deep with the diameter of 1.78 cm vertically into the bedding architecture in the z-stress direction from the center of the top face (**Figure 1**). Afterwards, an L-shape casing with outer diameter of 1.27 cm was bonded into the borehole using high-strength cold weld 2-part epoxy, leaving a 5.08 cm long uncased / open hole bottom section in the center of the cubic shale samples.

Shale sample 1, shown in **Figure 1**, has distinguishable laminations with two major horizontal interfaces appearing on faces 1-4. Also, there are two white calcite-filled / strongly bonded vertical fractures which can be seen on faces 1, 3, 5, and 6.

Shale sample 2 has one major horizontal interface, which connects with a nearly vertical fracture on face 2, as shown in **Figure 2** (left). Combining faces 1, 2, and 6, it can be seen that the interface-fracture structure severs a pentahedral corner from the block.

On shale sample 3 in **Figure 2** (right), both high permeability horizontal interfaces and vertical fractures cross through the cube. The white traces and braids on the block faces are foraminifera or *Inoceramid* shell fragments of relatively large size and small oyster and pelecypod shell fragments deformed during sedimentation (O'Neal 2007). Samples 4 and 5 in **Figure 3** exhibit high permeability according to pressure decay curves. To better imitate varied bonding strength of preexisting fractures and interfaces, we injected epoxy through the borehole to seal these preexisting fractures in shale samples 3-5; epoxy was seen seeping out of several points on the block faces and then injection was stopped. Residual epoxy in the borehole was washed out by rinsing the borehole with acetone 5 times. The epoxy formula has a nominal tensile strength of 1500 psi after setting for 12 hours. After injecting the epoxy, we left these three shale samples at room conditions to cure for more than 3 days before any further treatments.

Experimental procedures

On each of the first four shale samples, we conducted pre-injection characterization, CO_2 injection, post-injection characterization, and gas fracturing. Photography, acoustic wave, and

pressure decay tests were employed to characterize the shale samples before and after CO_2 injection-induced fracturing. Details of acoustic wave measurements and pressure decay tests can be found in Cha et al. (2014) and Wang et al. (2016). Before CO_2 injection, we first pre-heated the shale sample in an oven to 60 °C, which is above the supercritical temperature, then we set up the sample in the tri-axial loading frame (Cha et al. 2016) with injection pipelines connected. Afterwards, $scCO_2$ was pumped into the borehole until the sample was fractured. According to the borehole pressure when the samples were fractured, CO_2 in the borehole could be either in supercritical or gas state. After post-injection characterization, dye solution was injected at low pressure to color the induced fractures (Yao et al. 2017) and finally the samples were broken down by gas fracturing under tri-axial stresses to disclose the induced fracture planes (Alqahtani et al. 2016). For each shale sample, the experimental procedures slightly varied but generally followed:

1. Photograph sample faces,
2. Pre-injection acoustic wave measurements,
3. Pressure decay under no stress loading using 100 psig nitrogen gas,
4. CO_2 injection until the sample is fractured,
5. Photograph if induced fractures appear on sample faces,
6. Post-injection acoustic wave measurements,
7. Pressure decay under no stress loading using 100 psig nitrogen gas,
8. Fracture coloring by pressurizing dye solution into the borehole,
9. Nitrogen gas fracturing under tri-axial stresses,
10. Photograph sample faces and disclosed fracture planes.

Results and discussion

Supercritical CO_2 was injected to induce fracturing on four shale samples (#1-4) with borehole temperature above the supercritical temperature, and slick-water was injected to fracture one sample (#5) as a control experiment. The actual borehole pressure, depending on the breakdown point of the samples, was either above or below the supercritical pressure. Thus, these four samples were fractured by either gas CO_2 or $scCO_2$. Injection rate was adjusted in practical needs for each sample using an ISCO 500D syringe pump. Tri-axial stress loading levels and differences were varied to investigate the effect of *in-situ* stress on the breakdown pressure of CO_2 injection. The preexisting fracture types and the experimental conditions for five shale samples are listed in .

Pressure and temperature during $scCO_2$ injection

Under tri-axial stresses, $scCO_2$ was injected into the borehole and the borehole pressure and temperature were detected by a pressure transducer and a thermocouple in real-time. Tri-axial stresses were maintained at quasi-steady state by occasionally pressurizing air hydraulic pumps. The accuracy of the pressure transducer and thermocouple are ± 0.25% and ± 0.5°C in the experimental measurement range, respectively. The accuracy of pressure readings from the

air hydraulic pumps used for tri-axial stress loading is ± 0.5%. All these experimental parameters were recorded by a data acquisition unit operating at a frequency of two data points per second.

Shale sample 1 was fractured using $scCO_2$ under tri-axial stresses of x:y:z = 1600:2100:2600 psi, as shown in **Figure 4**. The injection rate was set at a constant rate of 40 ml/min. **Figure 5** presents the pressure and temperature profiles during CO_2 injection into shale sample 1. The breakdown pressure of CO_2 injection is 1300.1 psig at 1135.6 seconds, corresponding to an obvious bump on the x-stress and slight drops on y- and z-stress in **Figure 4**, indicating that new fractures were induced against the minimum horizontal stress. The temperature when the sample was fractured was 37.4 °C, then it sharply dropped to 29.4 °C due to $scCO_2$ leakage through generated fractures and subsequent expansion and vaporization.

Shale sample 2 was treated by injecting CO_2 into borehole under tri-axial stresses of x:y:z = 1100:1600:2100 psi (**Figure 6**). The borehole pressure and temperature profiles are shown in **Figure 7**. The first peak pressure is 953.6 psig at 191.1 seconds, achieved by opening the valve to allow $scCO_2$ to flow and expand from pump to borehole. At this point, the temperature was 46.2 °C. Then the pump was started at 10 ml/min while the borehole pressure kept decreasing rapidly. The pump rate was later increased to 40 ml/min, but the pressure decline rate only slowed down very slightly. Hence, we increased the pump rate to 80 ml/min, which increased the borehole pressure and reached a second peak of 727.2 psig at 907.6 seconds when the pump ran out of CO_2. The pump was then refilled and heated, during which borehole pressure decreased to 220.4 psig at 1608.6 seconds. In view of the high pressure decline rate, conductive fractures were present or likely generated and leakage occurred through these fractures. Then, pumping restarted at 80 ml/min, the third peak pressure is 769.3 psig at 1687.6 seconds. After finishing injecting the second pump of CO_2, the borehole pressure was allowed to decrease until 3000 seconds. During the whole injection process, there are no obvious responses on tri-axial stress curves in **Figure 6**, suggesting that fractures were created along the preexisting fractures or interfaces. At the moments when the first and the third pressure peaks were achieved, borehole temperature showed obvious decreases due to CO_2 leakage and resultant expansion. Since the pressure peaks are below the supercritical pressure of 1070.4 psi, shale sample 2 was fractured by gas CO_2.

Sample 3 was fractured by injecting $scCO_2$ under a tri-axial loading of x:y:z = 1100:1600:2100 psi (**Figure 8**). We injected two cycles of CO_2 to fracture sample 3, corresponding to two pressure peaks in **Figure 9**. At the beginning, after opening valve at 608.2 seconds, the borehole pressure rose to 766.4 psig. The initial injection rate was set at 40 ml/min and the pressure tended to level out. Thereafter the injection rate was increased to 80 ml/min, as $scCO_2$ ran out, the first pressure peak of 1392.5 psig was achieved at 1138.5 seconds with borehole temperature of 39.7 °C. The pump was refilled and heated, and then injection continued

at 80 ml/min. Borehole pressure reached the second peak of 1109.7 psig at 1722.5 seconds with borehole temperature of 35.4°C. On the temperature profile, there are two relatively small drops corresponding to these two injection cycles. However, on the stress profiles no obvious responses showed up, indicating that no big new fractures were created or $scCO_2$ just leaked off through the preexisting fractures sealed by epoxy.

Sample 4 was treated by injecting CO_2 into borehole under tri-axial stresses of x:y:z = 1200:2100:3000 psi, as shown in **Figure 10**. The injection pressure and borehole temperature profiles are shown in **Figure 11**. After completely opening the valve at 114.6 seconds, sample 4 was fractured at 804.3 psig with borehole temperature of 54.0 °C. This peak pressure corresponds to a very slight bump on x-stress loading in **Figure 10**, indicating that the gas CO_2 fracturing primarily occurred along preexisting fracture planes with possible new fractures created against x-stress. In addition, the temperature drastically dropped about 7 °C right after the fracturing, due to CO_2 leakage, expansion, and vaporization.

Under tri-axial loading of x:y:z= 1100:1600:2100 psi (**Figure 12**), shale sample 5 was fractured by injecting a synthetic slick-water which consisted of 0.1 wt% hydrolyzed polyacrylamide, 2.0 wt% KCl, and red dye. At 20 °C, the viscosity of this synthetic slick-water, measured with a rotating cylinder viscometer, is 1.8 mPa·s. **Figure 13** shows the borehole pressure profile during the slick-water injection. Injection started at 1 ml/min, and pressure reached the first peak of 521.3 psig at 1281.1 seconds. Ten seconds later, the pump was stopped to allow pressure drawdown. Seeing that borehole pressure leveled out near 100 psig, we restarted the pump at 1 ml/min, and the pressure reached the highest peak of 1602.5 psig at 2352.6 seconds. After 10 seconds, the pump was again stopped. Unexpectedly, file corrupted around 2500 seconds and the data acquisition system was restarted. This caused the data gaps in both **Figure 12** and **Figure 13**. As pressure leveled out near 180 psig, the pump was restarted at 1 ml/min, and a small peak of 309.7 psig was achieved at 3562.2 seconds, then pressure slowly decreased, suggesting the fracture propagation stage. Later, we increased the injection rate to 10 ml/min, and a pressure peak of 434.7 psig was reached at 4256.2 seconds. In tens of seconds, fluid leak off was observed on the sample faces and pump was turned off. On the tri-axial stress curves, there are slight responses on x-, y-, and z-stress corresponding to the last pressure peak, while all earlier pressure peaks including the highest one did not bring about any obvious responses. This suggests that probably only the last peak created new fractures or extended preexisting fractures, whereas all other peaks only broke through the weakly bonded preexisting fractures.

In comparison with shale samples 1-4 fractured by CO_2, slick-water fracturing needs extra hundreds of psi to break down the sample, even though originally shale sample 5 has more permeable fractures than others.

Active acoustic wave measurements

Active acoustic wave measurement is a nondestructive method to detect the internal structure changes of an object. Before and after CO_2 injection-induced fracturing, acoustic wave measurements were conducted on each pair of opposite faces of the shale sample to examine whether there are new fractures induced across the acoustic wave pathways. New fractures or gas gaps generated inside rock blocks generally dissipate acoustic energy density by means of retarding the acoustic wave velocity and reducing the wave amplitude, whereas tri-axial stress loading without sensible internal damage would only slightly change the wave velocity (Wang et al. 2017). **Figure 14** sketches the acoustic wave measurement locations for placing the acoustic transmitter on faces 1 and 5, and face 2 has the same numbering as face 1. The acoustic receiver was placed on corresponding locations on the opposite faces. In each acoustic measurement, 5000 data points were acquired for plotting the waveform.

P and S wave signatures measured from faces 1 and 3 for sample 1 before (black) and after (red) $scCO_2$ injection-induced fracturing are shown in **Figure 15** and **Figure 16**, respectively. All acoustic waveforms are normalized by the maximum peak-to-peak amplitude of the acoustic waves measured before $scCO_2$ injection. After induced fracturing, all locations show significant reduction in wave amplitude except 9 and 10, indicating that big fractures trespassing locations 1-8 and 11-12 were generated between faces 1 and 3.

P and S waves measured from faces 2 and 4 are normalized by the maximum peak-to-peak amplitude of the acoustic waves measured before $scCO_2$ injection, as shown in **Figure 17** and **Figure 18**, respectively. At locations 3-5 and 11, both P and S wave signatures have been dramatically damped as compared to their counterparts measured before $scCO_2$ injection at the same locations, indicating that induced fractures were generated along the acoustic transmission pathways of these measurement locations. Combining with the acoustic signatures on faces 1 and 3, it can be inferred that a big fracture that is slightly sinuous across the locations 3-5 of faces 2 and 4 between faces 1 and 3 was radially generated from the open hole section of the cubic shale sample. Location 11 suggests an extension of a branch fracture from the major fracture.

Figure 19 and **Figure 20** show the normalized signatures of P and S waves measured from faces 5 and 6 of sample 1, respectively. Before injection, amplitudes of signals from locations 1-4 are much smaller than those from locations 5-8, suggesting that the horizontal interfaces between these locations were open or weakly bonded. After injection-induced fracturing, all acoustic signatures of P and S waves, except 6 and 8, changed remarkably in both waveform and arrival time, indicating that these preexisting interfaces were further widened.

Shale samples 3-5 were first treated by injecting epoxy to seal the preexisting fractures and interfaces, and then acoustic wave was employed to evaluate the effectiveness of epoxy bonding. In **Figure 21**, all acoustic waves from faces 1 and 3 of sample 3 are normalized by the

maximum peak-to-peak amplitude of the acoustic waves measured after epoxy treatment. Acoustic measurements after epoxy treatment clearly showed that the P wave amplitudes were magnified and arrival times were shifted earlier, at locations 1-8 and 11 in particular. This is an indicator that injected epoxy has solidified in the preexisting fractures extending across these locations, which facilitated the transmission of acoustic waves. After $scCO_2$ injection-induced fracturing, the P wave signatures were again substantially attenuated in amplitude and retarded in arrival time due to reopened and / or newly generated fractures. Comparison of active acoustic waves effectively captured these changes of fractures inside nontransparent shale samples after each treatment.

Here for the sake of brevity, other acoustic data for shale samples 2-5 are omitted.

Borehole pressure decay curves

Borehole pressure decay is a direct indicator of the permeability of shale cubes. Before and after CO_2 injection-induced fracturing, we conducted pressure decay tests by first pressurizing the borehole to 100 psig and then allowing it to draw down to quantify the contribution of induced fractures to sample permeability. For shale samples 3-5, pressure decay tests were also used to evaluate the effectiveness of epoxy bonding of preexisting fractures and interfaces.

Pressure decay curves measured before and after CO_2 injection for shale sample 1 are compared in **Figure 22**. Before injection-induced fracturing, pressure decay is very slow, indicating that there were no preexisting fractures connecting the borehole to the outer faces. After fracturing, borehole pressure decreased from 100 to 0 psig in only a few seconds, which shows a significant permeability increase in the shale block due to injection-induced fractures.

Pressure decay curves measured before and after CO_2 injection for sample 2 are compared in **Figure 23**, demonstrating obvious permeability increase due to injection-induced fractures. Before injection, although there were a few big fractures appearing on the cube faces, pressure decay is very slow. Apparently, they were not connected to the borehole. As compared to sample 1, the decline rate after fracturing, however, is much slower, indicating that the induced fractures are much smaller or more confined than those generated in sample 1.

Figure 24 compares the pressure decay curves before and after the epoxy treatment of preexisting fractures in shale sample 3, showing that the fractures connecting to the borehole have been successfully sealed, at least in the near borehole region. The pressure decay curve measured after CO_2 injection demonstrated that the gas leak rate significantly increased due to fractures generated inside the shale cube.

Similar to shale sample 3, preexisting fractures and interfaces in sample 4 were also first treated using epoxy, during which several locations along the preexisting horizontal fractures

showed epoxy seepage. **Figure 25** compares the pressure decay curves before and after the epoxy treatment, demonstrating that the fractures connecting to the borehole, at least in the near borehole region, have been successfully sealed. After CO_2 injection-induced fracturing, the borehole gas pressure dropped to atmosphere nearly instantaneously, and to increase the borehole pressure to 100 psig needed very high flow rate from the nitrogen gas cylinder.

Epoxy treatment of preexisting fractures in shale sample 5 was not successful. As indicated by the pressure decay curves in **Figure 26**, epoxy injection and solidification, rather than sealed the preexisting fractures, further widened them. The acoustic wave tests did show enhanced signal intensity after epoxy treatment though. One postulation is that the preexisting fracture planes had been severely weathered and thus were abundant with weakly attached or freely movable shale fines, which undermined the consolidation effect of epoxy in the fractures. The pressure decay rate after slick-water injection significantly accelerated, due to fractures reopened or generated inside the shale cube.

Injection-induced fracture morphology

After pressure decay tests, dye solution was injected into the borehole at low pressure to color the injection-induced fractures. Finally, the shale samples were broken down by high-pressure nitrogen gas under tri-axial stresses to disclose the injection-induced fractures.

The assembled faces after dye injection and the fracture planes after gas breakdown of shale sample 1 are shown in **Figure 27**. After $scCO_2$ injection (left), vertical fractures denoted by yellow dashed lines that are generally perpendicular to the minimum horizontal stress (i.e. x-stress applied on faces 1 and 3) appeared on faces 2 and 6. Blue dye seeped out of the induced fractures and stained on the sample faces. After gas breakdown (right), the cross section shows only one big circular fracture induced by $scCO_2$ injection, which is sinuous around the open hole section. Fracture propagation, reflected by the plane smoothness, was barely affected by the calcite-filled fractures. The demarcation of $scCO_2$ fracture and nitrogen gas fracture (red curve) is quite clear, as can be identified from the transition of the relatively smooth to ragged planes. There are no secondary fractures seen in the picture except that nitrogen gas created an additional fracture along the bedding interface above the open hole section. Also note that the limited propagation of the fracture plane to the upper corners in the right corresponds to the least changes in acoustic signatures in **Figure 15** and **Figure 16**.

Comparing the faces of sample 2 after CO_2 injection to its original faces in **Figure 2** does not show any new fractures on all six faces, so the pictures are not included here. Nonetheless, the pressure decay test after CO_2 injection revealed a few gas leaking points along the preexisting fractures on faces 1 (numbered #2) and 2, as denoted in **Figure 28** (left). Thus, fractures were primarily induced along the weakly bonded preexisting fractures during CO_2 injection.

Pressurized up to 200 psig, penetration of the blue dye solution from the open hole into the shale matrix is still quite confined, as circled by the red curves in **Figure 28** (right), indicating that the induced fractures are too tight or thin for liquid to flow deeply into over the timescale of the injection. Considering the gas leaking traces (left), dye coloring, as an effective means for fracture visualization, underestimated the extension of the CO_2 injection-induced fractures. The gas fracture mainly opened along the pentahedral bubbling traces. It is necessary to point out that the major pentahedral fracture (right, upper) does not directly cut through the open hole section but is connected to it via a small horizontal fracture (right, lower), which corresponds to the very slow pressure decay curve measured initially before CO_2 injection. The small horizontal fracture, against the maximum vertical stress, was induced along the weak bedding interface. This discontinuity is also responsible for the poor injectivity of the blue dye solution. Induced fracturing of sample 2 demonstrated that when there are weakly bonded or open preexisting fractures, CO_2 pressurized in the open hole would preferentially break into and extend these fractures.

As shown in **Figure 2**, originally shale sample 3 has more preexisting vertical fractures on faces 1, 3, 5, and 6 than faces 2 and 4, on which the maximum horizontal stress was applied. So there is a high tendency that vertical fractures could be initially induced on faces 1, 3, 5, and 6. **Figure 29** (left) shows the faces of sample 3 after epoxy treatment and CO_2 injection. Dark epoxy stains can be seen on faces 1 (numbered #3) and 4, but no new induced fractures were observed on six faces. After dye injection, purple color seeped out of induced fractures on faces 1, 3, and 6, which are generally overlapping with preexisting fractures.

High-pressure nitrogen gas finally broke the sample down, disclosing the fracture planes inside the sample, as shown in **Figure 29** (right), based on which several aspects of the experiments are made clear. Note that a and b were opened from face 1, a was broken into c, which was further broken into d. First, one preexisting vertical fracture and one horizontal interface that had been bonded by epoxy are identified, as circled by the green dashed lines. Basically, the preexisting vertical fracture (a and b) corresponds to the epoxy stains on face 1, and the horizontal interface (d) corresponds to the stains on face 4 in **Figure 29** (left). Second, $scCO_2$ injection-induced fractures preferentially initiated and propagated along the preexisting fractures, even they were bonded with epoxy, as evidenced by the purple color over all epoxy stained areas. The probable reasons for $scCO_2$ breaking through the epoxy bonded fractures are that the preexisting fracture planes are not clean or consolidated enough to enable the nominal tensile strength of 1500 psi with the epoxy solution, due to detachable fines on the weathered preexisting fracture planes and / or epoxy shrinkage during solidification. And under a relatively small stress difference of 500 psi, they are still weak planes to be split. Third, the small colored fracture perpendicular to faces 1 and 3 (i.e. minimum horizontal stress direction) as circled by the closed red curve in **Figure 29** c (left), is a new fracture induced by $scCO_2$ injection under tri-

axial stresses, because there are no epoxy stains on it. Nitrogen gas fracturing further extended these induced fractures and opened other preexisting fractures, which are mostly either parallel or perpendicular to the minimum horizontal stress. Therefore, under a stress difference of 500 psi, preexisting fractures, even being weakly bonded, still dominated the scCO_2 injection-induced fracturing process.

When red dye solution was injected into shale sample 4 to color the CO_2 injection-induced fractures without any pressurization, it flowed out of the continuous preexisting horizontal fractures in the middle of the sample and the downturned fractures that newly appeared on the lower halves of faces 1 and 3, as shown in **Figure 30** (left). The sample was later broken down by high-pressure nitrogen gas under no tri-axial loading, as shown in **Figure 30** (right), which was taken by placing borehole to the left and opening face 2.

As can be seen from the cross section, the epoxy had covered the whole horizontal fracture plane at the middle of the z-axis, which was also indicated by the enhanced acoustic intensity measured after epoxy treatment. However, different from newly cracked planes, slight rubbing smeared these horizontal fracture planes very easily (a and b), meaning that this preexisting horizontal fractures is severely weathered and contains abundant detachable fines. Furthermore, the fines on the fracture planes could be responsible for the failing of epoxy bonding, which did not effectively prevent the CO_2 break through. Red color all over the horizontal plane verified that CO_2 preferentially reopened this weakly bonded plane by conquering the z-stress. In **Figure 30** c (right), there is a newly generated fracture, which was not stained with epoxy but was colored by red dye. It dips with an angle of about 45° to the horizontal plane, and along its tip, gas fracturing further reached the bottom face 6.

These observations suggest that CO_2 injection-induced fractures preferentially initiate and propagate in the weakly bonded preexisting fractures, even if they are opening against the maximum vertical z-stress. Meanwhile, under the high stress difference of 900 psi, new fractures can be induced against the horizontal stresses. That is, weakly bonded preexisting fractures and *in-situ* stress with high contrast compete to dominate the CO_2 injection-induced fracturing process.

During slick-water fracturing of shale sample 5, red slick-water seeped out of faces 1, 3, 4, and 5 from preexisting fractures (yellow dashed lines), but there are no noticeable new fractures generated on the sample faces, as shown in **Figure 31** (left). On the fracture planes in **Figure 31** (right), epoxy covered the fractures near the borehole (green dashed lines), which are also colored by slick-water, verifying that slick-water preferentially flowed into the epoxy bonded preexisting fractures. The red curve circles the revealed slick-water fracture plane based on coloring and seepage. Other major fracture planes without color were created by nitrogen gas fracturing, they are generally perpendicular to either x-stress or y-stress. Similar to shale samples

2 and 3, with a stress difference of 500 psi, preexisting fractures dominated the slick-water fracturing initiation and propagation.

The surface conditions of preexisting and newly generated fractures were examined using an Olympus BX60 microscope, as shown in **Figure 32**. Both the preexisting and new fracture surfaces, before examination, were cleaned by blowing high rate air. As is obvious, the preexisting fracture surface has many more fines that seem readily detachable than the newly generated fracture surface, which corroborates the speculation that the preexisting fractures are severely weathered and detachable fines are responsible for the defective epoxy bonding between the fracture planes.

Experimental results of four shale samples fractured by supercritical or gas CO_2 and one fractured by slick-water are summarized in **Table 2**, including tri-axial stress conditions, breakdown pressure and temperature, stress responses to breakdown pressures during injection, N_2 gas fracturing peak pressures under tri-axial stresses, and brief description of injection-induced fracture morphology and orientation.

Breakdown pressure analyses

Breakdown pressure refers to the peak pressure during fluid injection, which can be predicted using equation (1) or (2) based on different assumptions of rock properties. However, to open a preexisting fracture, the injection pressure only needs to counterbalance the *in-situ* stress applied on the fracture planes. Although permeability of Niobrara shale is very low, on the order of 10 micro-Darcy (Yao, 2016), equation (1) obviously overestimates the breakdown pressures by a large proportion, so it is not used here.

With typical Biot's coefficient and Poisson's ratio (Maldonado et al. 2011, Yao et al. 2016) as well as real tri-axial stress readings and reasonably assigned tensile strength, breakdown pressures of shale samples 1-4 are predicted using equation (2), as compared with experimental values in . But still, the experimental breakdown pressures are overestimated for samples 1, 2, and 4, even assuming zero tensile strength. Two major contributing factors are the low viscosity of CO_2 and the preexisting fractures, which together eased the fracture initiation. Specifically, the nonconformable preexisting fractures in samples 2 and 3, as shown in **Figure 28** (right) and **Figure 29** (right), could possibly sidestep under tri-axial stresses to generate high stress anisotropy or even unloading regions around the nonconformity. In addition, decreasing tri-axial stress levels and increasing stress differences should be favorable for reducing breakdown pressures, e.g. samples 1 vs. 2 and samples 1-3 vs. 4, respectively. Nonetheless, sample 3 deviated from the declining trend with a depressed stress level relative to sample 1 owing to uncertainties of epoxy bonding strength and the irregularities of preexisting fractures.

The breakdown pressure of sample 3 can be perfectly matched by assigning a tensile strength of 442 psi; however, it should be noted that the major fracture plane of sample 3 in **Figure 29** (right) is perpendicular to the maximum horizontal stress, which is contradictory with linear elastic assumptions of equation (2). Similarly, assigning a tensile strength of 700 psi engenders a perfect match for sample 5; nonetheless, the major fracture plane in **Figure 31** (right) is also perpendicular to the maximum horizontal stress. Seeing that in both samples 3 and 5, induced fractures were predominantly initiated along weakly bonded preexisting fractures, the measured breakdown pressures are essentially the opening pressures of these preexisting fractures that are perpendicular to the maximum horizontal stress. That is, their breakdown pressures should approximate the applied y-stresses. Comparing with the *in-situ* y-stress, measured breakdown pressure of sample 3 is 14.4% lower, and that of sample 5 is only 3.4% lower, the difference between which should be attributed to the viscosity disparity of $scCO_2$ and slick-water.

Therefore, in contrast with poroelastic breakdown pressure model and slick-water injection-induced fracturing, gas CO_2 and $scCO_2$ tend to induce fracturing in shale samples of all three types of preexisting fractures at much lower injection pressures, which could even be lower than the minimum horizontal stress.

Conclusions

In consideration of safe and permanent CO_2 geological sequestration and storage in aquifers and depleted oil and gas reservoirs underlying caprocks with faults, weak interfaces, and natural or artificial fractures, we experimentally investigated the gas and supercritical CO_2 injection-induced fracturing processes in shale rocks with strongly and weakly bonded fractures under varied tri-axial stresses. Based on experimental observations, we can draw the following conclusions.

1) For borehole injection without pore pressure, gas or supercritical CO_2 induced fractures initiated and propagated to the rock boundary instantly associated with temperature drops, due to low fluid viscosity as well as volume expansion and vaporization during leakage. CO_2 expansion helped alleviate fluid pressure drop and further promoted fracture propagation as the required propagation pressure decreases with enlarging fracture size.

2) Calcite-filled fractures that are strongly bonded with little variations in mineralogy on both sides almost have no influence on transverse fracturing induced by supercritical CO_2 injection. In shale samples with preexisting fractures that are weakly bonded or open, gas or supercritical CO_2 and slick-water injection preferentially opened or continued to extend the preexisting fractures, regardless of their orientations to the *in-situ* stresses. Given sufficiently high stress differences, new fractures perpendicular to the minimum horizontal stress can be generated.

3) Gas or supercritical CO_2 injection-induced fracturing of shale samples with strongly and weakly bonded fractures occurred at much lower breakdown pressures than both poroelastic model predictions and slick-water breakdown pressure, attributing to preexisting fractures and low viscosity of CO_2. In general, decreasing tri-axial stress levels and increasing stress differences lowered the breakdown pressure. Briefly, when the minimum horizontal stress is not perpendicular to the preexisting fractures, preexisting weak fractures and tri-axial stresses compete for the dominance of the injection-induced fracturing process.

4) Active acoustic wave measurements and borehole pressure decay tests provide effective but nondestructive means for qualitative and quantitative characterization of CO_2 injection-induced fractures in nontransparent shale samples.

This laboratory study with real shale rocks directly demonstrated the effect of preexisting fractures on CO_2 injection-induced fracturing processes in aquifer and reservoir caprocks. These experimental observations and quantitative assessments are critical for understanding and predicting geomechanical effects on field-scale CO_2 injection, flow, and storage as well as evaluating storage site selection, storage capacity, injection designs, and long term leakage risks in fractured aquifers and oil and gas reservoirs. These experimental achievements will be incorporated into reservoir simulators, such as TOUGH2-CSM (Winterfeld et al. 2012) and TOUGH-FLAC (Rutqvist 2011), to simulate field-scale CO_2 injection processes and guarantee safe and permanent storage in fractured reservoirs.

Acknowledgement

Financial supports from National Energy Technology Laboratory of US Department of Energy (Quantitative characterization of impacts of coupled geomechanics and flow on safe and permanent geological storage of CO_2 in fractured aquifers, Project number: DE-FE0023305) and Foundation CMG are greatly appreciated. The authors also thank CEMEX Lyons Plant for providing the shale rock samples.

Reference

Alqahtani, N. B., Cha, M., Yao, B., Yin, X., Kneafsey, T. J., Wang, L., Wu, Y.-S. and Miskimins, J. L., 2016, May. Experimental investigation of cryogenic fracturing of rock specimens under true triaxial confining stresses. In SPE Europec, featured at 78th EAGE Conference and Exhibition. SPE-180071-MS.

Bissell, R.C., Vasco, D.W., Atbi, M., Hamdani, M., Okwelegbe, M. and Goldwater, M.H., 2011. A full field simulation of the In Salah gas production and CO_2 storage project using a coupled geo-mechanical and thermal fluid flow simulator. Energy Procedia, 4, pp.3290-3297.

Buttinelli, M., Procesi, M., Cantucci, B., Quattrocchi, F. and Boschi, E., 2011. The geo-database of caprock quality and deep saline aquifers distribution for geological storage of CO_2 in Italy. Energy, 36(5), pp.2968-2983.

Cha, M., Alqahtani, N.B., Yao, B., Yin, X., Wu, Y.-S. and Kneafsey, T. J. 2016. Development of laboratory system for cryogenic fracturing study. Energy Geotechnics, pp. 381-388.

Cha, M., Yin, X., Kneafsey, T., Johanson, B., Alqahtani, N., Miskimins, J., Patterson, T. and Wu, Y.S., 2014. Cryogenic fracturing for reservoir stimulation–Laboratory studies. Journal of Petroleum Science and Engineering, 124, pp.436-450.

Chadwick, R.A., Arts, R., Eiken, O., Kirby, G.A., Lindeberg, E. and Zweigel, P., 2004. 4D Seismic Imaging of an Injected CO_2 Plume at the Sleipner Field, Central North Sea. Geological Society, London, Memoirs, 29(1), pp.311-320.

Chen, Y., Nagaya, Y. and Ishida, T., 2015. Observations of fractures induced by hydraulic fracturing in anisotropic granite. Rock Mechanics and Rock Engineering, 48(4), pp.1455-1461.

Cuéllar-Franca, R.M. and Azapagic, A., 2015. Carbon capture, storage and utilisation technologies: A critical analysis and comparison of their life cycle environmental impacts. Journal of CO_2 Utilization, 9, pp.82-102.

Detournay, E. and Cheng, A., 1992, January. Influence of pressurization rate on the magnitude of the breakdown pressure. In the 33th US Symposium on Rock Mechanics. American Rock Mechanics Association.

Esposito, R., Harvick, C., Shaw, R., Mooneyhan, D., Trautz, R. and Hill, G., 2013. Integration of pipeline operations sourced with CO_2 captured at a coal-fired power plant and injected for geological storage: SECARB phase III CCS demonstration. Energy Procedia 37: 3068-3088.

Global CCS Institute (GCI), <https://www.globalccsinstitute.com/projects/sleipner%C2%A0co2-storage-project>, retrieved by June 6, 2017.

Global CCS Institute (GCI), June, 2016. Introduction to industrial carbon capture and storage. Global Status of CCS: special report.

Haimson, B. and Fairhurst, C., 1967. Initiation and extension of hydraulic fractures in rocks. SPE Journal, 7(03), pp.310-318.

Huang, Z.Q., Winterfeld, P.H., Xiong, Y., Wu, Y.-S. and Yao, J., 2015. Parallel simulation of fully-coupled thermal-hydro-mechanical processes in CO_2 leakage through fluid-driven fracture zones. International Journal of Greenhouse Gas Control, 34, pp.39-51.

Hubbert, M.K. and Willis, D.G., 1972. Mechanics of hydraulic fracturing, pp.239-257.

Iding, M. and Ringrose, P., 2010. Evaluating the impact of fractures on the performance of the In Salah CO_2 storage site. International Journal of Greenhouse Gas Control, 4(2), pp.242-248.

Iribarren, D., Petrakopoulou, F. and Dufour, J., 2013. Environmental and thermodynamic evaluation of CO_2 capture, transport and storage with and without enhanced resource recovery. Energy, 50, pp.477-485.

Irwin, G.R., 1957. Analysis of stresses and strains near the end of a crack traversing a plate. Presented at the Applied Mechanics Division Summer Conference, Berkeley, California, June 13-15. American Society of Mechanical Engineers.

Ishida, T., Aoyagi, K., Niwa, T., Chen, Y., Murata, S., Chen, Q. and Nakayama, Y., 2012. Acoustic emission monitoring of hydraulic fracturing laboratory experiment with supercritical and liquid CO_2. Geophysical Research Letters, 39(16).

Ishida, T., Chen, Y., Bennour, Z., Yamashita, H., Inui, S., Nagaya, Y., Naoi, M., Chen, Q., Nakayama, Y. and Nagano, Y., 2016. Features of CO_2 fracturing deduced from acoustic emission and microscopy in laboratory experiments. Journal of Geophysical Research: Solid Earth, 121(11), pp.8080-8098.

Koperna, Jr., G. J., Kuuskraa, V., Riestenberg, D., Rhudy, R., Trautz, R., Hill, G. and Esposito, R., 2013. The SECARB anthropogenic test: status from the field. Energy Procedia 37: 6273-6286.

Li, X., Feng, Z., Han, G., Elsworth, D., Marone, C., Saffer, D. and Cheon, D.S., 2016. Breakdown pressure and fracture surface morphology of hydraulic fracturing in shale with H_2O, CO_2 and N_2. Geomechanics and Geophysics for Geo-Energy and Geo-Resources, 2(2), pp.63-76.

Liu, C., 2016. Optimizing hydraulic fracture spacing and lateral well spacing in tight/unconventional resource development through fully coupling stress shadowing effects and fluid flow: an integrated approach. Doctoral dissertation, Colorado School of Mines.

Mondal, M.K., Balsora, H.K. and Varshney, P., 2012. Progress and trends in CO_2 capture/separation technologies: a review. Energy, 46(1), pp.431-441.

Oye, V., Aker, E., Daley, T.M., Kühn, D., Bohloli, B. and Korneev, V., 2013. Microseismic monitoring and interpretation of injection data from the In Salah CO_2 storage site (Krechba), Algeria. Energy Procedia, 37, pp.4191-4198.

O'Neal, D.L., 2015. Chemostratigraphic and depositional characterization of the Niobrara Formation, CEMEX Quarry, Lyons, CO. Master's Thesis dissertation, Colorado School of Mines.

Pan, P.Z., Rutqvist, J., Feng, X.T. and Yan, F., 2013. Modeling of caprock discontinuous fracturing during CO_2 injection into a deep brine aquifer. International Journal of Greenhouse Gas Control, 19, pp.559-575.

Pham, V.T.H., Riis, F., Gjeldvik, I.T., Halland, E.K., Tappel, I.M. and Aagaard, P., 2013. Assessment of CO_2 injection into the south Utsira-Skade aquifer, the North Sea, Norway. Energy, 55, pp.529-540.

Rinaldi, A.P., Rutqvist, J. and Cappa, F., 2014. Geomechanical effects on CO_2 leakage through fault zones during large-scale underground injection. International Journal of Greenhouse Gas Control, 20, pp.117-131.

Ringrose, P.S., Mathieson, A.S., Wright, I.W., Selama, F., Hansen, O., Bissell, R., Saoula, N. and Midgley, J., 2013. The In Salah CO_2 storage project: lessons learned and knowledge transfer. Energy Procedia, 37, pp.6226-6236.

Rutqvist, J., Vasco, D.W. and Myer, L., 2010. Coupled reservoir-geomechanical analysis of CO_2 injection and ground deformations at In Salah, Algeria. International Journal of Greenhouse Gas Control, 4(2), pp.225-230.

Suehiro, Y., Nakajima, M., Yamada, K. and Uematsu, M., 1996. Critical parameters of $\{xCO_2+(1-x)\ CHF_3\}$ for x = (1.0000, 0.7496, 0.5013, and 0.2522). The Journal of Chemical Thermodynamics, 28(10), pp. 1153-1164.

Tyler, L.D. and Vollendorf, W.C., 1975, January. Physical observations and mapping of cracks resulting from hydraulic fracturing in situ stress measurements. In Fall Meeting of the Society of Petroleum Engineers of AIME. SPE-5542-MS.

Vasco, D.W., Rucci, A., Ferretti, A., Novali, F., Bissell, R.C., Ringrose, P.S., Mathieson, A.S. and Wright, I.W., 2010. Satellite-based measurements of surface deformation reveal fluid flow associated with the geological storage of carbon dioxide. Geophysical Research Letters, 37(3).

Vilarrasa, V. and Carrera, J., 2015. Geologic carbon storage is unlikely to trigger large earthquakes and reactivate faults through which CO_2 could leak. Proceedings of the National Academy of Sciences, 112(19), pp.5938-5943.

Vulin, D., Kurevija, T. and Kolenkovic, I., 2012. The effect of mechanical rock properties on CO_2 storage capacity. Energy, 45(1), pp.512-518.

Wang, L., Yao, B., Cha, M., Alqahtani, N.B., Patterson, T.W., Kneafsey, T.J., Miskimins, J.L., Yin, X. and Wu, Y.-S., 2016. Waterless fracturing technologies for unconventional reservoirs-opportunities for liquid nitrogen. Journal of Natural Gas Science and Engineering, 35, pp.160-174.

Wang, L., Yao, B., Xie, H., Kneafsey, T.J., Winterfeld, P.H., Yin, X. and Wu, Y.S., 2017. Experimental investigation of injection-induced fracturing during supercritical CO_2 sequestration. International Journal of Greenhouse Gas Control, 63, pp.107-117.

White, J.A., Chiaramonte, L., Ezzedine, S., Foxall, W., Hao, Y., Ramirez, A. and McNab, W., 2014. Geomechanical behavior of the reservoir and caprock system at the In Salah CO_2 storage project. Proceedings of the National Academy of Sciences, 111(24), pp.8747-8752.

Yao, B., 2016. Experimental study and numerical modeling of cryogenic fracturing process on laboratory-scale rock and concrete samples. Master's Thesis, Colorado School of Mines.

Yao, B., Wang, L., Patterson, T., Kneafsey, T.J., Yin, X. and Wu, Y.-S., 2017. Experimental study and modeling of cryogenic fracturing treatment of synthetic rock samples using liquid nitrogen under tri-axial stresses. In SPE Unconventional Resources Conference, 15-16 February, Calgary, Alberta, Canada. SPE 185050.

Zhang, R., Yin, X., Winterfeld, P.H. and Wu, Y.S., 2016. A fully coupled thermal-hydrological-mechanical-chemical model for CO_2 geological sequestration. Journal of Natural Gas Science and Engineering, 28, pp.280-304.

Zhang, X., Lu, Y., Tang, J., Zhou, Z. and Liao, Y., 2017. Experimental study on fracture initiation and propagation in shale using supercritical carbon dioxide fracturing. Fuel, 190, pp.370-378.

Zhao, C., Chen, X. and Zhao, C., 2012. K_2CO_3/Al_2O_3 for capturing CO_2 in flue gas from power plants. Part 1: Carbonation behaviors of K_2CO_3/Al_2O_3. Energy & Fuels, 26(2), pp.1401-1405.

Zhao, C., Chen, X., Zhao, C., Wu, Y. and Dong, W., 2012. K_2CO_3/Al_2O_3 for capturing CO_2 in flue gas from power plants. Part 3: CO_2 capture behaviors of K_2CO_3/Al_2O_3 in a bubbling fluidized-bed reactor. Energy & Fuels, 26(5), pp.3062-3068.

Zoback, M.D. and Gorelick, S.M., 2012. Earthquake triggering and large-scale geologic storage of carbon dioxide. Proceedings of the National Academy of Sciences, 109(26), pp.10164-10168.

Zweigel, P., Arts, R., Lothe, A.E. and Lindeberg, E.B., 2004. Reservoir geology of the Utsira Formation at the first industrial-scale underground CO_2 storage site (Sleipner area, North Sea). Geological Society, London, Special Publications, 233(1), pp.165-180.

Figures

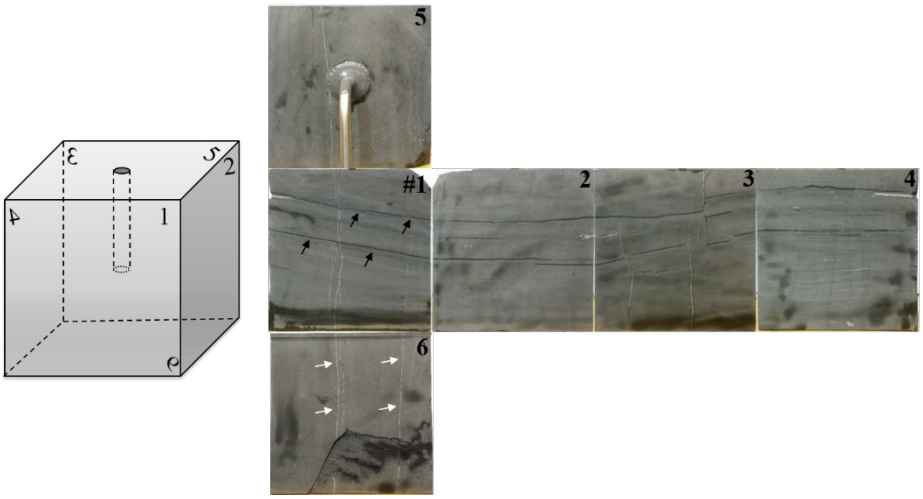

Figure 1. Unfolded faces of sample 1 before CO_2 injection-induced fracturing. Slightly inclined and horizontal dark lines are preexisting bedding interfaces (black arrows), vertical white stripes are calcite-filled fractures (white arrows), and dark areas are residual stains of water used for color contrast during photographing faces. A thin piece lost from face 6, uneven stress loading was mitigated by using Teflon plate shims during the experiments.

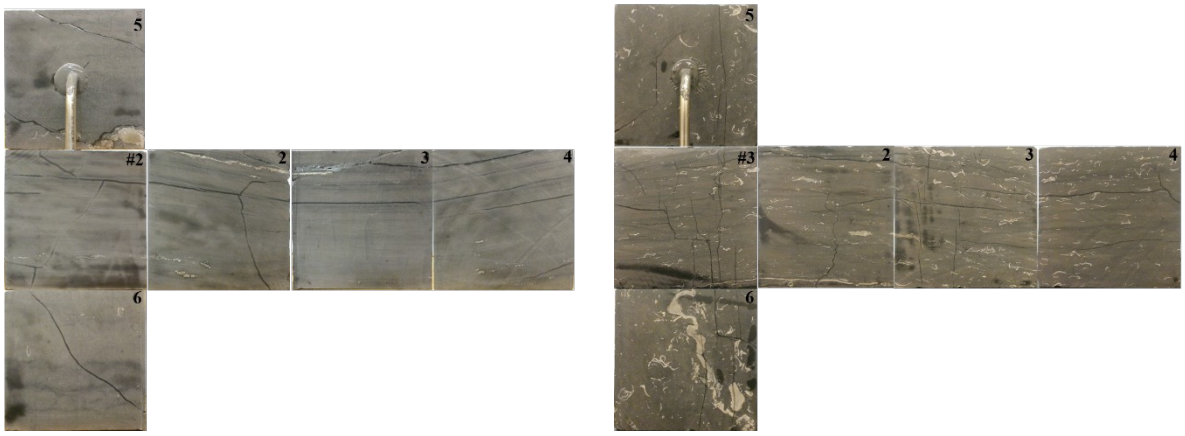

Figure 2. Faces of samples 2 (left) and 3 (right) before CO_2 injection-induced fracturing. Note: the block number (e.g. #2) is on face 1 of each block. Dark lines are preexisting fractures. The loose triangular piece on the upper corners of faces 2, 3, and 5 was attached by high-strength cold weld 2-part epoxy (left). White clusters on sample 3 are deformed shell fragments (right).

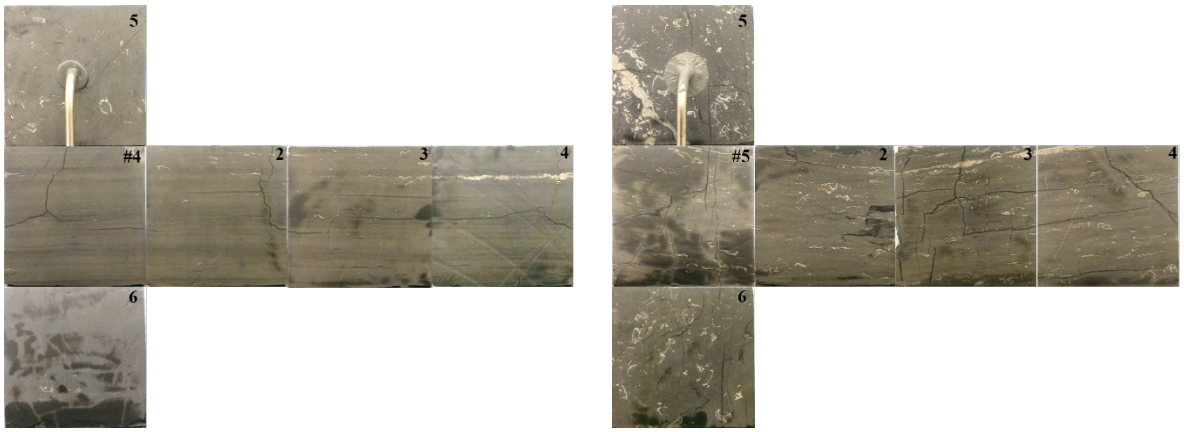

Figure 3. Faces of samples 4 (left) and 5 (right) before injection-induced fracturing. Note: the block number (e.g. #4) is on face 1 of each block. Dark lines are preexisting fractures, dark areas are residual stains of water used for color contrast during photographing faces. White clusters on sample faces are deformed shell fragments (right).

Figure 4. Tri-axial stresses for CO_2 injection into shale sample 1.

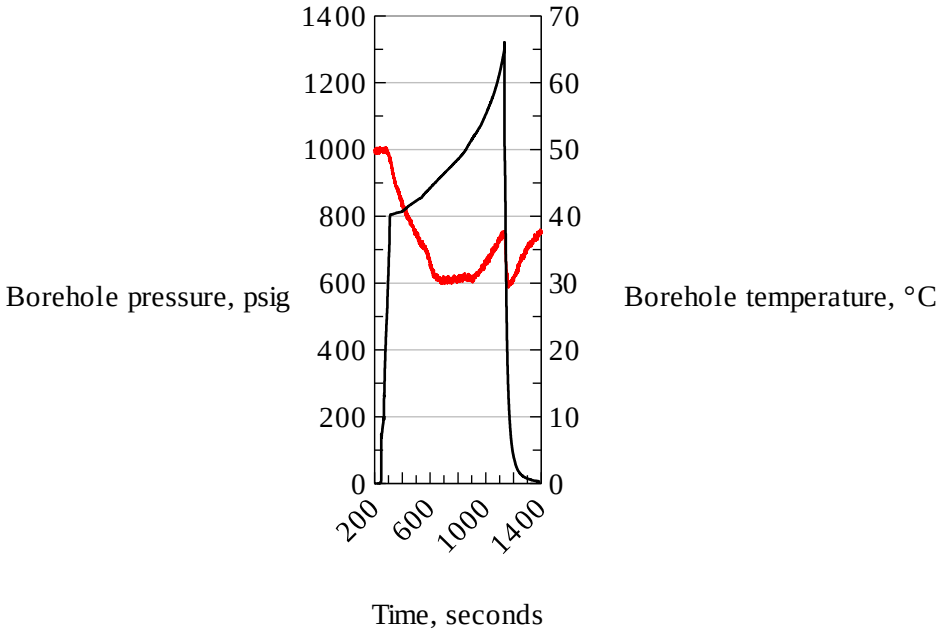

Figure 5. Borehole pressure (black) and temperature (red) during CO_2 injection into shale sample 1.

Figure 6. Tri-axial stresses for CO_2 injection into sample 2.

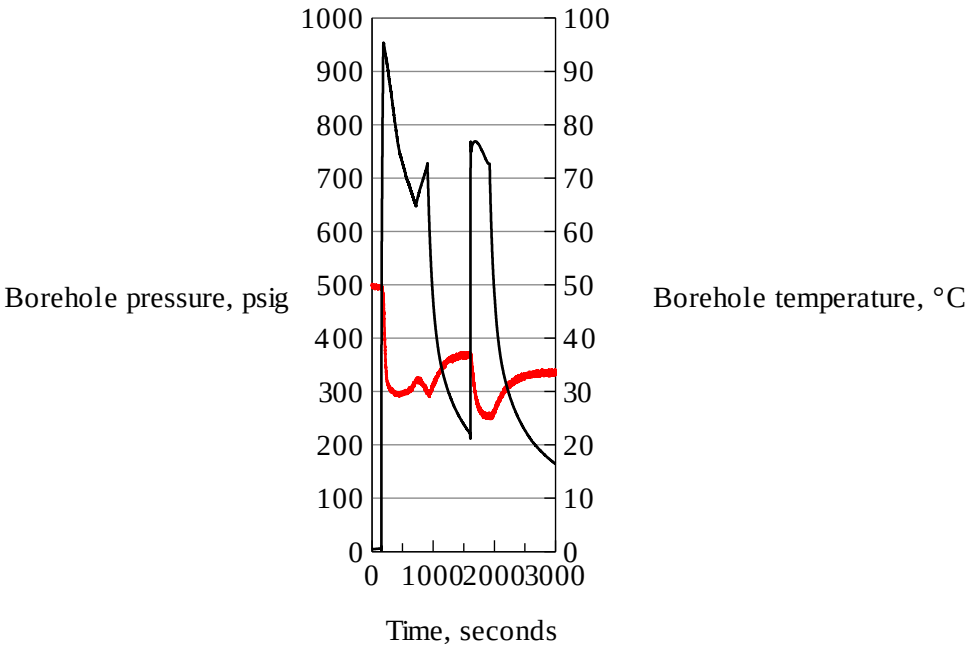

Figure 7. Borehole pressure and temperature during CO_2 injection into sample 2.

Figure 8. Tri-axial stresses for scCO_2 injection into sample 3.

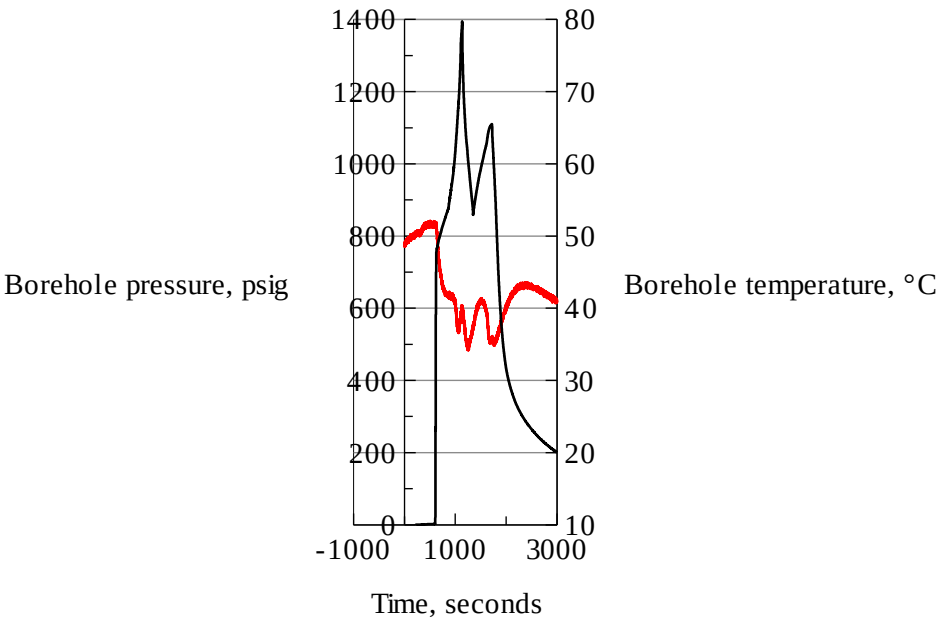

Figure 9. Borehole pressure and temperature during CO_2 injection into sample 3.

Figure 10. Tri-axial stresses for CO_2 injection into sample 4.

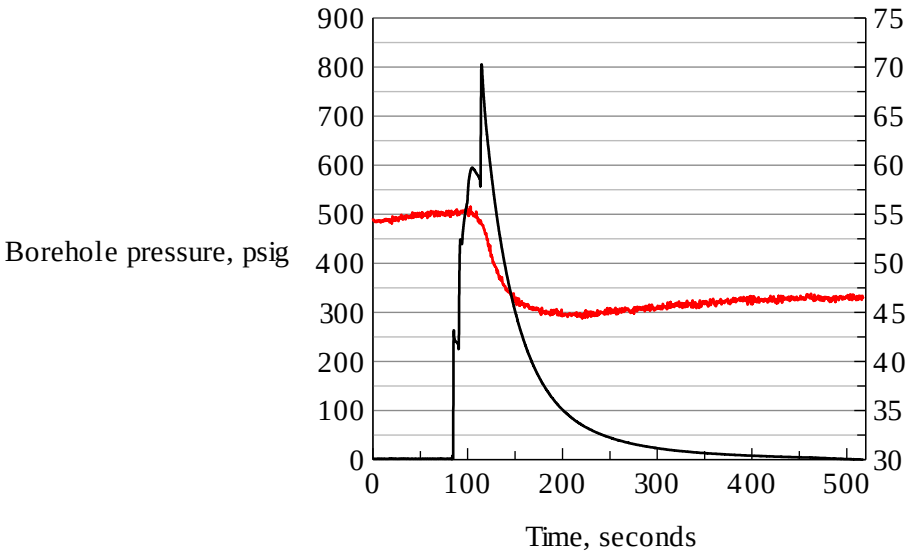

Figure 11. Pressure and temperature during CO_2 injection into sample 4.

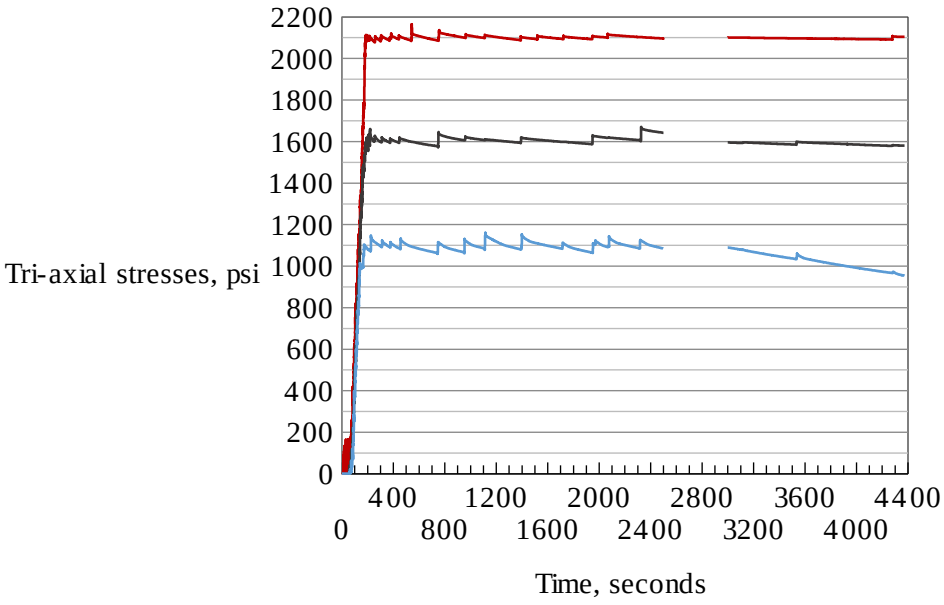

Figure 12. Tri-axial tresses for slick-water injection into sample 5.

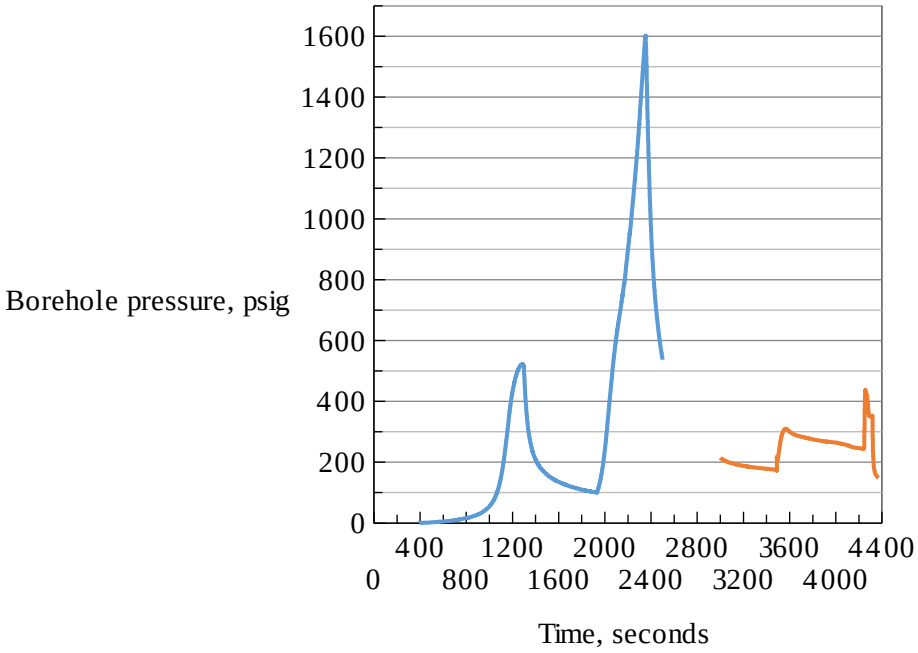

Figure 13. Slick-water injection pressure for sample 5.

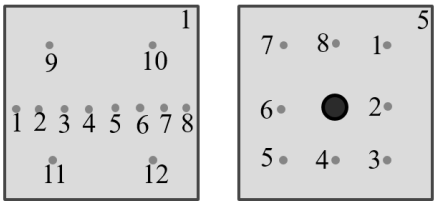

Figure 14. Acoustic wave measurement locations (small dots) on faces 1 and 5.

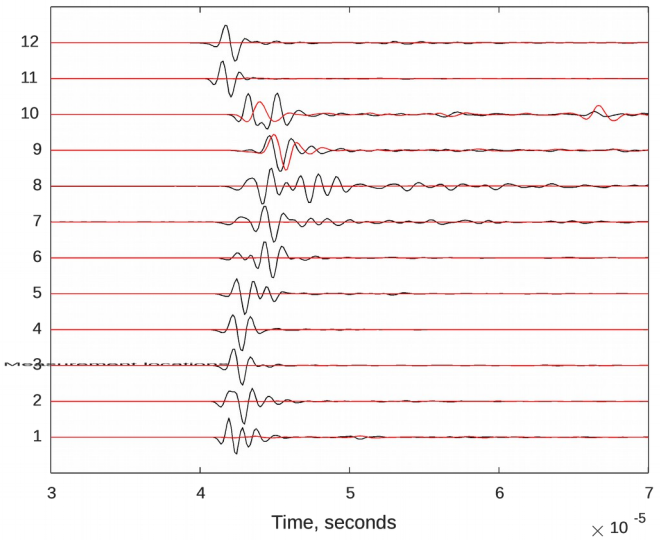

Figure 15. P-wave signatures measured before (black) and after (red) $scCO_2$ injection from faces 1 and 3 of sample 1.

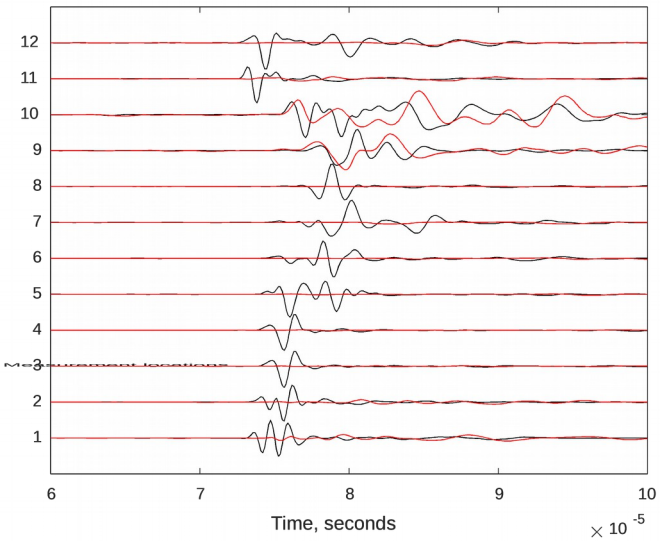

Figure 16. S-wave signatures measured before (black) and after (red) $scCO_2$ injection from faces 1 and 3 of sample 1.

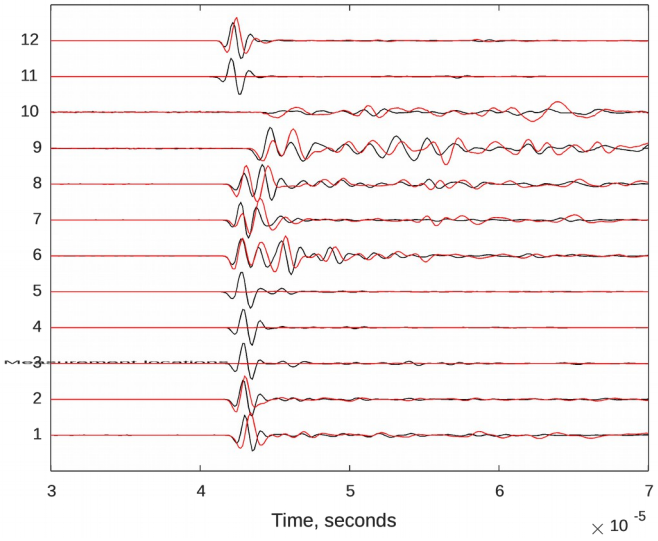

Figure 17. P-wave signatures measured before (black) and after (red) $scCO_2$ injection from faces 2 and 4 of sample 1.

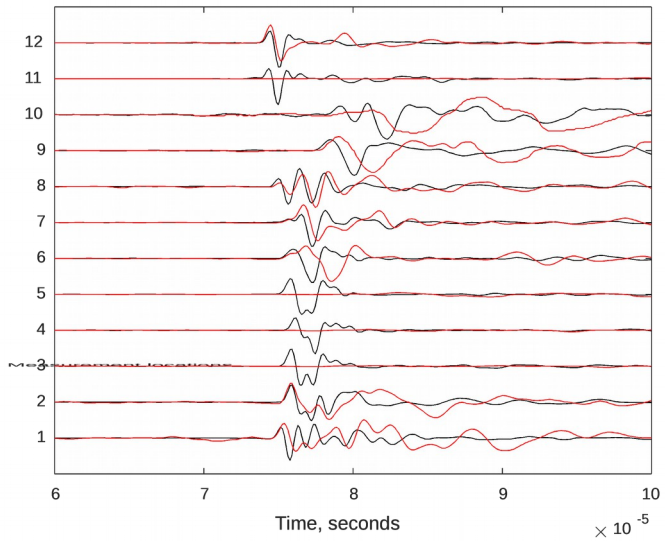

Figure 18. S-wave signatures measured before (black) and after (red) $scCO_2$ injection from faces 2 and 4 of sample 1.

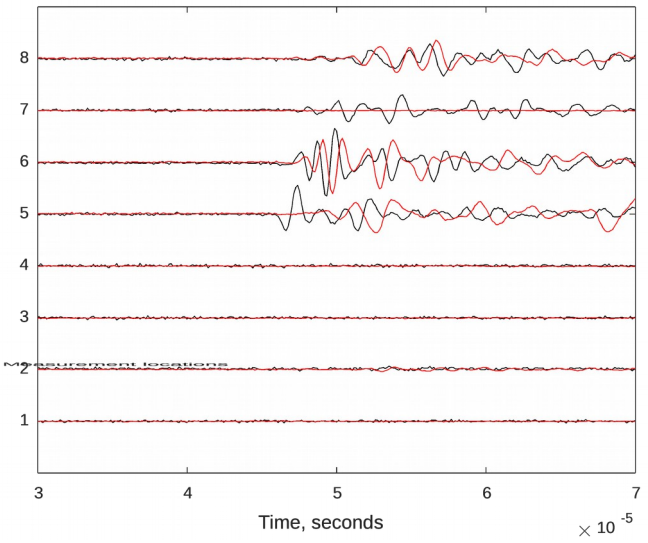

Figure 19. P-wave signatures measured before (black) and after (red) $scCO_2$ injection from faces 5 and 6 of sample 1.

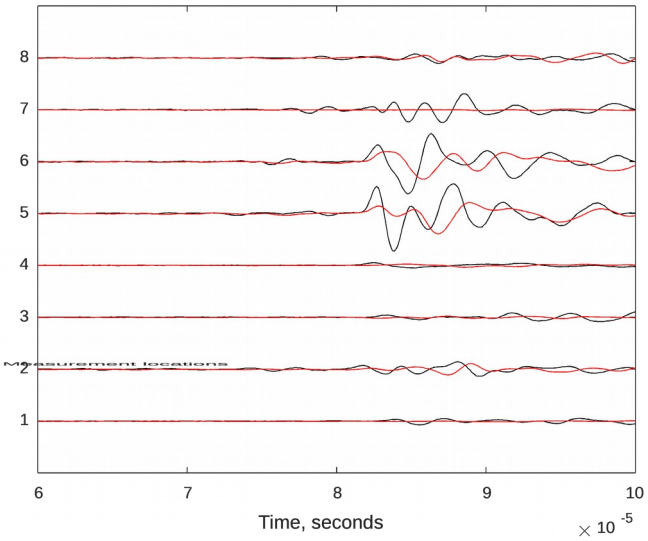

Figure 20. S-wave signatures measured before (black) and after (red) $scCO_2$ injection from faces 5 and 6 of sample 1.

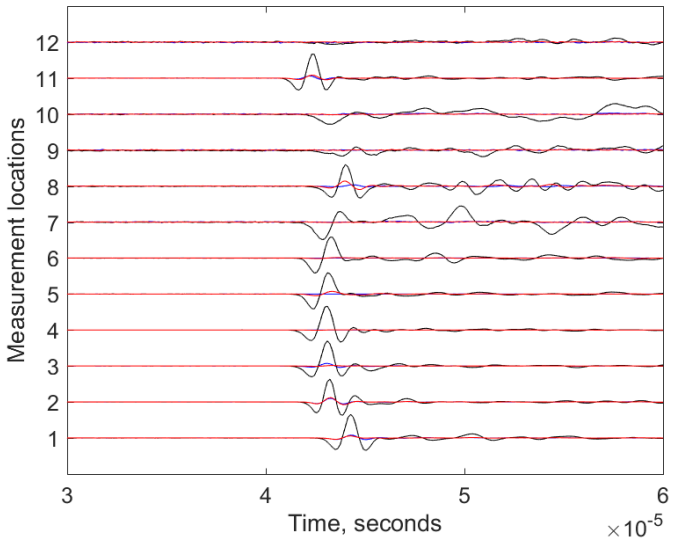

Figure 21. P-wave signatures measured before (blue) and after epoxy treatment (black), and after CO_2 injection-induced fracturing (red) from faces 1 and 3 of shale sample 3.

Figure 22. Pressure decay curves before and after injection-induced fracturing of sample 1.

Figure 23. Pressure decay curves before and after CO_2 injection for sample 2.

Figure 24. Pressure decay curves before and after epoxy treatment of preexisting fractures, and after CO_2 injection for sample 3.

Figure 25. Pressure decay curves before and after epoxy treatment of preexisting fractures, and after CO_2 injection for shale sample 4.

Figure 26. Pressure decay curves before and after epoxy treatment of preexisting fractures, and after slick-water injection for shale sample 5.

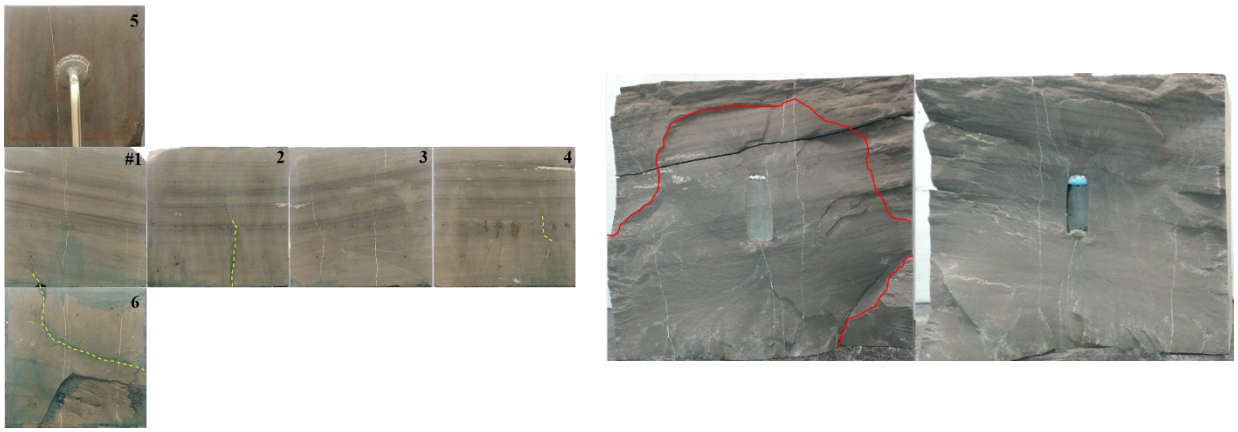

Figure 27. Faces of sample 1 after blue dye coloring and $scCO_2$ injection-induced fracture morphology (unfolded from face 2) after gas breakdown. Yellow dashed lines denote the appeared induced fractures (left) and red curves demarcate the inner $scCO_2$ induced fracture and outer gas fracture planes.

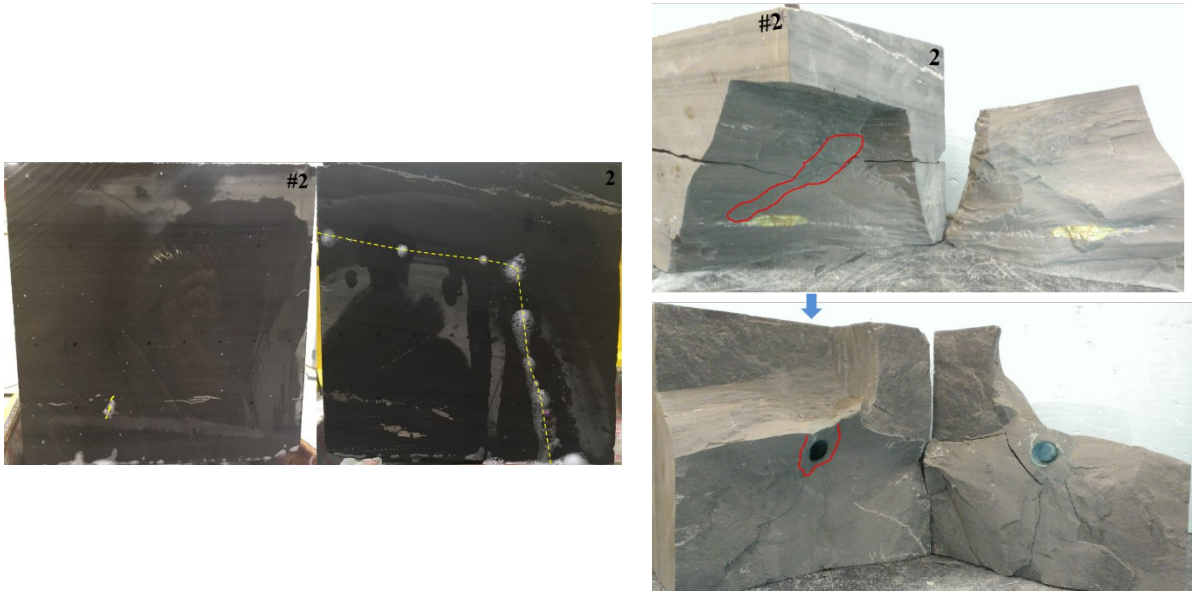

Figure 28. Leaking points on faces 1 (numbered #2) and 2 during pressure decay after CO_2 injection align on preexisting fractures highlighted by yellow dashed lines (left), and CO_2 injection-induced fractures circled by red curves (right) of sample 2. The golden mineral is pyrite.

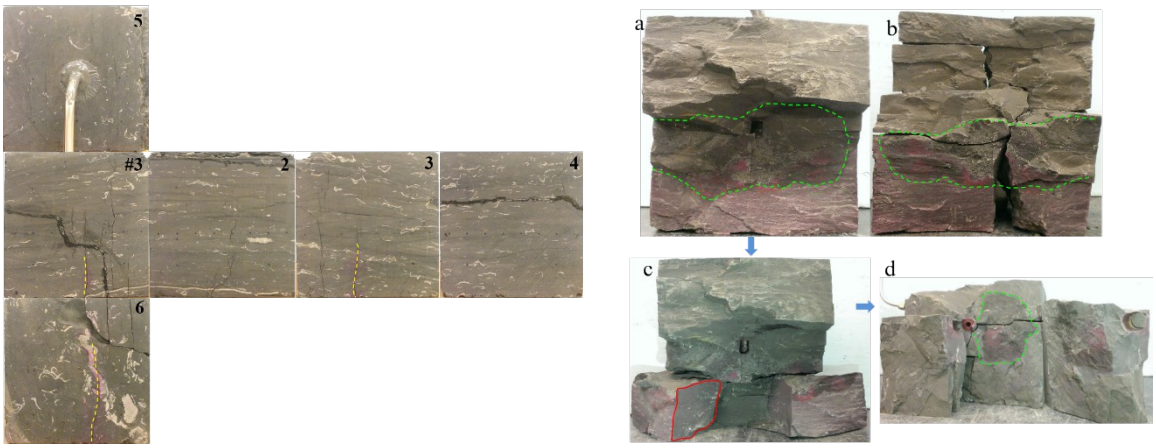

Figure 29. Faces of sample 3 after dye injection (left) and $scCO_2$ injection-induced fracture planes (right, a and b) unfolded from face 1. In the left image, dark stains on faces 1 (numbered #3) and 4 are epoxy, yellow dashed lines denote the induced fractures; in the right image, green dashed lines circle the areas covered by epoxy, red color denotes the induced fracture planes, the closed red curve indicates a new fracture perpendicular to the minimum horizontal stress.

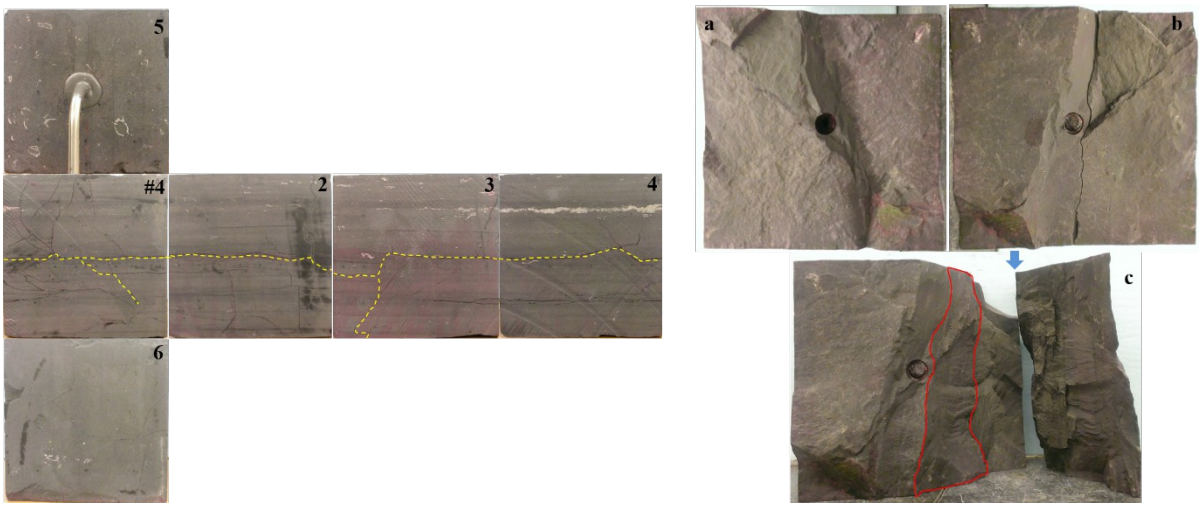

Figure 30. Faces of sample 4 after dye injection and fracture morphology after gas breakdown (unfolded from face 2 by placing borehole to the left). Yellow dashed lines denote the major induced fracture along the preexisting horizontal interface and the newly created downward fracture, as is circled by the red curve in c, red color (right) covers the induced fracture planes.

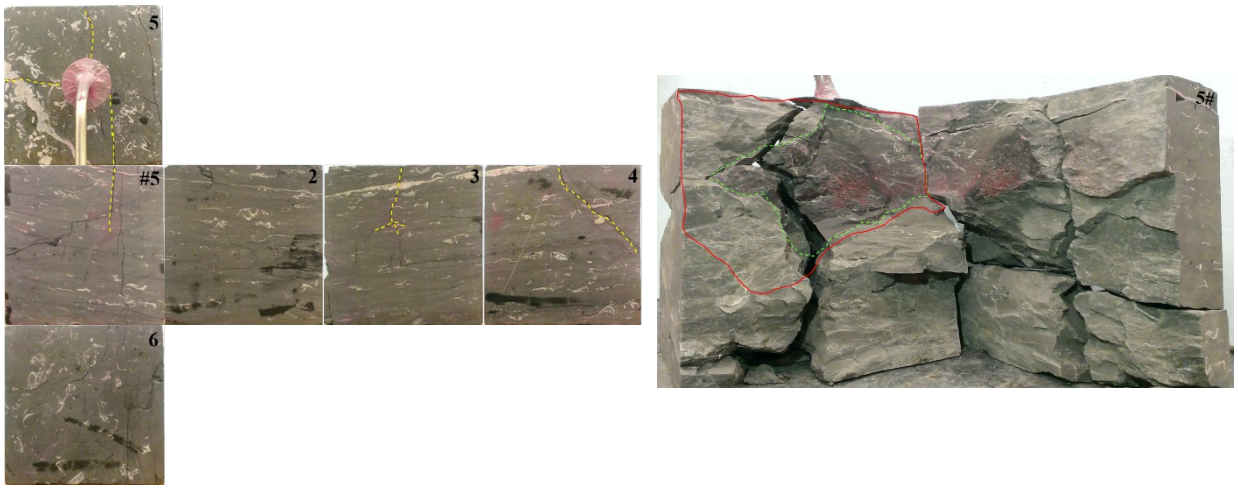

Figure 31. Faces of sample 5 after slick-water fracturing (left) and fracture morphology after gas breakdown. Yellow dashed lines denote the reopened preexisting fractures (left), green dashed lines indicate the epoxy stained area, red curves circle the revealed slick-water fracture plane.

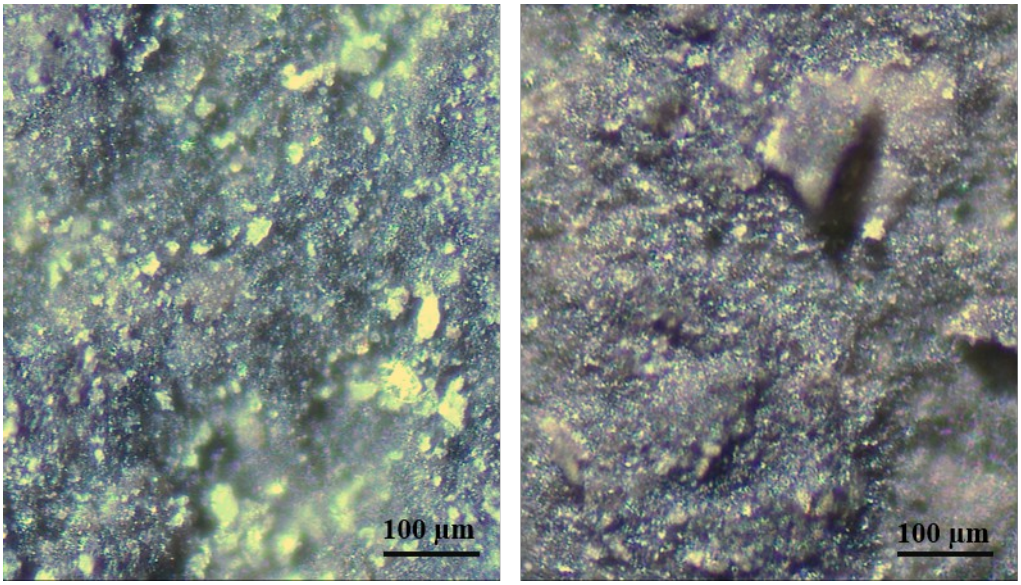

Figure 32. Microscopic surface conditions of preexisting (left) and newly generated (right) fractures from shale sample 5. The green-yellow dots in the left image represent detachable fine particles.

Tables

Table 1. Experimental conditions of CO_2 / slick-water injection for five shale samples

shale #	injected fluid	tri-axial stresses x:y:z psi	stress difference psi	injection rate ml/min	preexisting fracture types
1	$scCO_2$	1600:2100:2600	500	40	calcite-filled, strongly bonded
2	gas CO_2	1100:1600:2100	500	80	weakly bonded / open fractures
3	$scCO_2$	1100:1600:2100	500	80	weakly epoxy bonded
4	gas CO_2	1200:2100:3000	900	open valve	weakly epoxy bonded
5	slick-water	1100:1600:2100	500	1	weakly epoxy bonded

Table 2. Summary of CO_2 / slick-water injection-induced fracturing for shale samples

shale #	injected fluid, ml/min	tri-axial stress x:y:z psi	P_b, psig T, °C	T drop, stress response	N_2 P_b	Induced fracture orientation and morphology
1	$scCO_2$, 40	1600:2100 : 2600	1300.1, 37.4	Yes, obvious	1448.0	Big radial and sinuous fracture around borehole, ⊥x-stress
2	gas CO_2, 80	1100:1600 : 2100	953.6, 46.2	Yes, not obvious	1715.5	Tiny fractures connected to unbonded preexisting fractures and interfaces
3	$scCO_2$, 80	1100:1600 : 2100	1392.5, 39.7	Yes, not obvious	2263.8	Reopened big weakly epoxy bonded fracture ⊥y-stress, and a small new fracture ⊥x-stress
4	gas CO_2, *	1200:2100 : 3000	804.3, 54.0	Yes, not obvious	1803.3	Reopened big weakly epoxy bonded interface ⊥z-stress, and a new fracture ~45° against y-stress
5	Slick-water, 1	1100:1600 : 2100	1602.5, 19.6	No, not obvious	1316.4	Reopened big weakly epoxy bonded fracture ⊥y-stress, and a small one ~45° against x-stress

Note: *-fractured when valve was opened; P_b-breakdown pressure with an accuracy of ± 0.25%; T-temperature with an accuracy of ± 0.5ºC; ⊥-perpendicular to.

Table 3. Matching of measured breakdown pressures with equation (2)

shale #	tri-axial stresses x:y:z psi	tensile strength psi		P_b from eqn. (2)	measured P_b exp.	Deviation %
1	1603.7:2101.7:2595.1	0	Biot's constant	1823.6	1300.1	-28.7
2	1065.3:1585.3:2094.4	0	α = 0.9	1084.1	953.6	-12.0
3	1073.4:1593.2:2095.6	442		1392.6	1392.5	0.0
4	1220.4:2082.2:2999.7	0	Poisson's ratio	1062.8	804.3	-24.3
		700	υ			
5	1112.8:1657.5:2101.5		= 0.3	1602.5	1602.5	0.0

Note: the accuracy of tri-axial stresses is ± 0.5%.